International Journal of Hydrogen Energy 60 (2024) 1224–1238

Contents lists available at ScienceDirect

International Journal of Hydrogen Energy

journal homepage: www.elsevier.com/locate/he

Experimental study of cycle-by-cycle variations in a spark ignition internal combustion engine fueled with hydrogen

Naqash Azeem [a,b,*], Carlo Beatrice [b], Alberto Vassallo [c], Francesco Pesce [c], Davide Gessaroli [c], Clemens Biet [d], Chiara Guido [b]

[a] University of Naples Parthenope, Naples, Italy
[b] National Research Council-Institute of Sciences and Technologies for Sustainable Energy and Mobility (CNR-STEMS), Naples, Italy
[c] Dumarey Automotive Italia S.p.A., Turin, Italy
[d] Technische Universität Berlin, Berlin, Germany

A B S T R A C T

High fluctuations in the combustion process from one cycle to another, referred to as cycle-by-cycle variations, can have adverse effects on internal combustion engine performances, particularly in spark ignition (SI) engines. These effects encompass incomplete combustion, the potential for misfires, and adverse impacts on fuel economy. Furthermore, the cycle-by-cycle variations can also affect a vehicle's drivability and overall comfort, especially when operating under lean-burn conditions. Although many cycle-by-cycle analyses have been investigated extensively in the past, there is limited in-depth knowledge available regarding the causes of cycle-by-cycle (CbC) variations in hydrogen lean-burn SI engines. Trying to contribute to this topic, the current study presents a comprehensive analysis of the CbC variations based on the cylinder pressure data. The study was carried out employing a hydrogen single-cylinder research SI engine. The experiments were performed by varying more than fifty operating conditions including the variations in lambda, spark advance, boost pressure, and exhaust gas recirculation, however, the load and speed were kept constant throughout the experimental campaign. The results indicate that pressure exhibits significant variations during the combustion process and minor variations during non-combustion processes. In the period from the inlet valve close till the start of combustion, pressure exhibits the least variations. The coefficient of variation of pressure (COV_P) curve depicts three important points in H2-ICE as well: global minima, global maxima, and second local minima. The magnitude of the COV_P curve changes across all the operating conditions, however, the shape of the COV_P curve remains unchanged across all the operating conditions, indicating its independence from the operating condition in an H2-ICE. This study presents an alternative approach for a quick combustion analysis of hydrogen engines. Without the need for more complex methodologies like heat release rate analysis, the presented cylinder pressure cycle-by-cycle analysis enables a quick and precise identification of primary combustion features (start of combustion, center of combustion, end of combustion, and operation condition stability). Additionally, the engine control unit could implement these procedures to automatically adjust cycle-by-cycle variations, therefore increasing engine efficiency.

1. Introduction

Even though fossil fuels today cover an important percentage of the world's global energy demand, the adverse impacts of their combustion—including acid rain, greenhouse gas, and other things that are hazardous to both humans and the environment— cannot be ignored. To this goal, the fast advancement of utilizing renewable energy is accelerating worldwide and gathering speed. Researchers have explored hydrogen as an alternative energy source to further enhance this progress and reduce emissions. The significant advantage of using a fuel cell to produce power from hydrogen is that it does not cause any significant local pollution; the only byproduct is water. A further benefit of hydrogen is its extraordinarily high specific gravimetric energy density, which may provide three times as much energy per unit mass as the burning of gasoline [1]. Local production of hydrogen can also reduce a country's dependency on foreign energy sources. In addition, a wide range of substances, such as water, gas, oil, sewage sludge, biofuels, and others, may be used to produce hydrogen [2]. In recent years, progress has been made in integrating hydrogen into power networks, encompassing a variety of topics from the production and storage of hydrogen to re-electrification and considerations of safety. Other sources provide in-depth descriptions of these developments, and various investigations are underway to characterize the present stage of development in hydrogen system integration utilizing cutting-edge techniques [3]. There is broad consensus that the production of hydrogen from renewable energy sources like solar and wind has great potential for furthering global sustainable development [4,5]. Furthermore, many scholars agreed that hydrogen represents the best choice selection for a chemical

* Via Guglielmo Marconi, 4, 80125 Napoli NA, Campania Italy.
E-mail addresses: naqash.azeem@stems.cnr.it, iamnaqash@hotmail.com, naqash.azeem001@studenti.uniparthenope.it (N. Azeem).

https://doi.org/10.1016/j.ijhydene.2024.02.182
Received 17 November 2023; Received in revised form 25 January 2024; Accepted 13 February 2024
Available online 26 February 2024

fuel for future global societies [6,7], it is a clean and efficient fuel [8,9]. Electricity and hydrogen have been envisioned for years as essential elements of a "hydrogen economy," functioning as complementing secondary carriers [10,11].

A significant trend for the transportation industry in the future is the adoption of hydrogen as a fuel for internal combustion engines (ICEs) or fuel cells. However, ICEs may be modified to operate on various fuels, achieving this requires optimizing the engine control unit carefully as well as making sure that all the materials used in the engine are compatible with the chosen fuels [12,13], common technical challenges are storage, injection, charging, combustion, NOx, knocking, and aftertreatment. Materials compatibility in ICEs fueled with hydrogen was evaluated and a critical assessment of their suitability for a safe and reliable operation was provided [14,15]. Multiple methods in the calculation of lambda were compared for ICE fueled with hydrogen and the results showed that processed UEGO lambda methodology is the closest to the reference Spindt-Brettschneider analysis [16]. The fuel cell (FC) technology and hydrogen as a fuel source for ICEs both are promising alternatives for mobility technology. The key benefits of hydrogen-fueled ICES are enhanced tolerance to contamination, reduced resource usage, the simplicity of converting ICES to operate on hydrogen [12,13,17–19], and especially total cost of ownership [20]. Research on hydrogen-fueled ICEs has been ongoing since the previous century [21–38]. Hydrogen-fueled ICE has the potential to have higher output power above a specific speed threshold [39]. As there is a need for fast replacement of fossil fuels, ICEs fueled by hydrogen have the potential to enter the market quickly, enabling practical deployment with minimal delay, especially if the use of diesel cars is gradually decreased in the upcoming years [36,37,40–43]. Exhaust emissions for a SI engine fueled with gasoline and industrial by-product hydrogen (IPH) were compared and the NOx emissions of the SI engine fueled with IPH were slightly increased, however, CO and HC emissions were reduced by more than 90% [44].

Spark ignition engines include cycle-by-cycle changes, which are more prominent when the mixture is lean or heavily diluted, such as when a high exhaust gas recirculation (EGR) ratio is employed [45]. Numerous prior studies on cycle-by-cycle variations in spark ignition engines found that these engine variations were mostly influenced by variations in the early combustion phase. Cycle-by-cycle variations in engines can be lowered by methods that enhance the rate of combustion of fuel-air combinations [45–51]. Cycle variations are a typical phenomenon in ICEs fueled with hydrogen as well. Researchers have shown that by reducing cycle fluctuations, it is possible to boost power output by 10% while keeping fuel consumption constant [53]. Therefore, reducing cycle-by-cycle variations in hydrogen engines is essential.

The effects of hydrogen energy share were analyzed for a SI engine fueled with natural gas, the CbC variations of the combustion duration was reduced by adding the hydrogen energy share [52]. The turbulent flame speed in stoichiometric mixtures of hydrocarbons and air is approximately 10 times larger than the laminar flame speed. In contrast, when employing standard engine spark timing for hydrogen-air mixtures, the turbulent flame speed is on the same order of magnitude (though somewhat higher) than the laminar flame speed [53]. These results indicate that hydrogen can increase the mixture's combustion velocity while also reducing the effect of turbulent flow variations on the combustion process. Cycle-by-cycle variability reduces because of the reduction in turbulent effects. An experimental study [54] on the effects of introducing hydrogen to a lean-burn natural gas spark ignition engine and concluded that doing so is a useful and efficient way to reduce cycle-by-cycle variability in lean-burn spark ignition engines. Using a 2.0L direct-injection hydrogen engine as the foundation, an experimental analysis of the cycle variation characteristics of direct-injection hydrogen engines was performed, cycle variations were investigated in relation to engine load & speed, ignition advance angle, equivalency ratio, and start of injection (SOI) [55]. The results based on the turbulent properties of local gas at the spark plug were presented to analyze the contribution of this mechanism to CbC variability in a SI lean methane-hydrogen blends engine and results concluded that this mechanism is much more important and it has primary effects on the flame propagation process [56]. CbC variations on a SI engine fueled with hydrogen and gasoline were tested under multiple hydrogen flow rates and it is concluded that the increase in the hydrogen flow rate increases the CbC variations [57]. A numerical approach was compared with experimental data for a SI engine fueled with three different hydrogen contents and results of COV of IMEP showed reasonable alignment with the measured data [58].

A more comprehensive experimental study should be conducted only on pure hydrogen and a wide range of engine operating conditions to evaluate the effects of operating conditions of ICEs fueled with hydrogen on cycle-by-cycle variations. This research presents in-cylinder pressure variations along with a comprehensive analysis of the coefficient of variation of pressure (COV_P) based on the pressure data acquired for 100 cycles against each crank angle with a time step of 0.2 CAD. This study allows fast and accurate detection of the main combustion features (start of combustion, center of combustion, end of combustion and operation condition stability) without the use of more complex procedures like the rate of heat release analysis. These procedures could be implemented in the engine control unit for the automatic control of cycle-by-cycle variations enhancing the efficiency of the engine. The experimental campaign was performed on a spark ignition internal combustion engine fueled with hydrogen designed by PUNCH Torino, details are explained in the next section, followed by the data visualization section in which some of the techniques for data visualization are explained. Results are presented and discussed in the last section of this article.

2. Experimental setup

The engine used in this article is designed by PUNCH Torino. It is a single-cylinder, 0.5-liter, four-stroke cycle engine, originally modified from a direct injection (DI) diesel engine to port fuel injection (PFI) with a spark plug and it is fueled by hydrogen. All the characteristics of the engine are tabulated in Table 1. The data was acquired with the test bench whose characteristics are presented in Table 2 and a schematic diagram of the test bench is presented in Fig. 1.

The engine was operated by swiping multiple operating conditions like lambda, spark advance, exhaust gas recirculation, and boost pressure. However, the speed and load were kept constant, 2000 RPM and full load, respectively (the choice should be motivated). The ranges of exhaust gas recirculation, boost pressure, lambda, and spark advance are tabulated in Table 3. The pressure data were acquired for 100 consecutive cycles with a time step of 0.2 CAD within the ranges of the operating conditions presented in Table 3.

3. Data visualization

The data acquired through the procedure explained in the previous section were visualized based on the following methods:

Table 1
Characteristics of internal combustion engine fueled with hydrogen.

Bore	83.0 mm
Stroke	90.4 mm
Unit Displacement	0.5 ℓ
CR	12.0
Piston Type	Hemi-spherical bowl, shallow
Intake Ports	Swirling, low turbulence
Spark-plug	Cold-type, low protrusion
Fuel System	PFI with rail, 6-8barREL feed pressure
Injector type	Solenoid, 'peak & hold', 2.2 g/s static flow @ 8 bar Delta Pressure
Valve phasing	IVO = 356 CAD, IVC = 592 CAD; EVO = 155 CAD, EVC = 392 CAD

Table 2
Characteristics of the test bench.

Part	Characteristic
Dyno	Horiba Dynas Low Inertia Max torque: 480Nm Max Power: 250 kW Max RPM: 10,000 RPM
Pressure transducer	Kistler Piezo-resistive, Type 6044A (0–200 bar) Linearity (at 23 °C): ≤ ± 0.3 % FSO (Full scale output) Sensitivity shift: ≤ ± 1 % Thermal shock error: ≤ ± 0.2 bar

Pressure versus crank angle: The cycle-by-cycle can be evaluated by analyzing the cylinder pressure traces of each cycle against the crank angle. The variation in pressure can be caused by the following factors:

- Rate of change in burning as well as volume.
- Variations in the combustion process relative to TDC (e.g., flame development angle).
- Variations in the magnitude of the heat release rate profile.
- Variations in the shape of the heat release rate profile.

As the variation in pressure represents changes in multiple factors, the visualization of pressure against crank angle during each cycle has the potential to reveal many insights. The ratio of standard deviation (σ) in pressure to the mean (μ) of pressure as shown in Equation (1) is called the coefficient of variation (COV) of Pressure (COV_P). The COV_P can play a vital role in analyzing cycle-by-cycle variations.

$$COV_P = \left(\frac{\sigma}{\mu}\right)_P \times 100 \tag{1}$$

Where: σ is the standard deviation and μ is the mean, which can be calculated from Equation (2) and Equation (3) respectively.

$$\sigma = \sqrt{\frac{1}{N=1}\sum_{i=1}^{n}(x_i - \mu)^2} \tag{2}$$

$$\mu = \frac{1}{N}\sum_{i=1}^{n} x_i \tag{3}$$

In this **article**, a detailed analysis of COV_P curve is performed including the calculation of ignition delay, first and second-half combustion, and total combustion duration by using the formulas shown in Equations (4)–(7).

$$Ignition\ delay = Angle\ of\ first\ minima - Angle\ of\ ignition \tag{4}$$

$$First\ half\ combustion = Angle\ of\ maxima - Angle\ of\ ignition \tag{5}$$

$$Second\ half\ combustion = Angle\ of\ second\ local\ minima - Angle\ of\ maxima \tag{5}$$

$$Combustion\ duration = Angle\ of\ second\ local\ minima - Angle\ of\ first\ minima \tag{7}$$

Indicated Mean Effective Pressure ($IMEP$)**:** The integration of the pressure versus crank angle curve throughout the complete cycle is known as indicated mean effective pressure (IMEP), the formula to calculate IMEP is shown in Equation (8).

$$IMEP = \int p\frac{dV}{V_d} \tag{8}$$

The ratio of standard deviation (σ) of IMEP to the mean (μ) of IMEP as shown in Equation (9) is called the coefficient of variation of IMEP (COV_{IMEP}). The COV_{IMEP} also has the potential to illustrate the variations occurring cycle-by-cycle.

$$COV_{IMEP} = \left(\frac{\sigma}{\mu}\right)_{IMEP} \times 100 \tag{9}$$

Table 3
Ranges of EGR, boost pressure, lambda, and spark advance.

EGR (%)	Boost Pressure (kPa)	Lambda	SA (CAD)
0 – 10	160 – 220	1.35 – 2.25	6 – 32

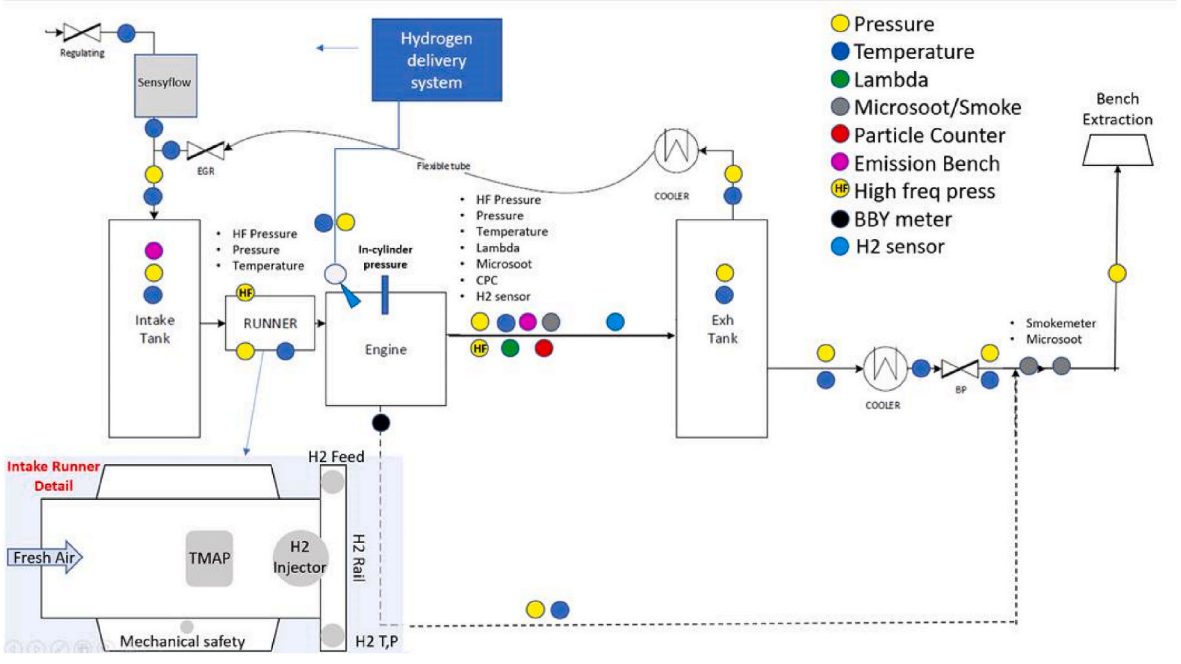

Fig. 1. Schematic of the test bench.

Where: σ is the standard deviation and μ is the mean, which can be calculated from Equation (2) and Equation (3) respectively.

Heat release curves: During the combustion process, the heat release by the fuel chemical energy is shown in Equation (7). However, Equation (7) includes the heat transfer and crevice terms as well. In the current article, the heat loss to the walls is calculated separately from the Woshni equation shown in Equation (8). Therefore, the heat release calculated from Equation (7) neglecting heat transfer and crevice terms is denoted as apparent heat release (HR_A). The heat loss to the walls calculated from Equation (8) is denoted as Q_W and combining these two as shown in Equation (11) is the total heat release denoted as HR_T.

$$\delta Q_{ch} = \left(\frac{c_v}{R}\right) V\, dp + \left(\frac{c_v}{R} + 1\right) p\, dV + (h' - u + c_v T)\, dm_{cr} + \delta Q_{ht} \tag{7}$$

Where: Q_{ch}, dm_{cr}, and Q_{ht} represent the fuel chemical energy release or gross heat release, the change in mass due to crevice effects and convective heat transfer, respectively.

$$Q_W = h_C \times A_W \times (T - T_W) \tag{8}$$

Where: h_C and A_W represent the heat transfer coefficient, the exposed combustion chamber surface area. The T and T_W are the instantaneous temperature of the cylinder gas and cylinder wall temperature, respectively. The formula to calculate h_C by the Woshni equation is shown in Equation (9).

$$h_c = 3.26\, B^{-0.2} \times p^{0.8} \times T^{-0.55} \times w^{0.8} \tag{9}$$

Where: B, p, T, and w represent bore in *meters*, pressure in *kPa*, and temperature in K, and gas velocity in m/s, respectively.

$$HR_T = HR_A + Q_W \tag{11}$$

Mass Fraction Burned (***MFB***)**:** The progress of combustion in terms of crank angle is demonstrated by the mass fraction burned (MFB). The thermal efficiency of the engine, maximum pressure and temperature of a cycle, and exhaust emissions are all significantly affected by the rate of combustion inside the engine cylinder. The MFB helps in quantifying this combustion rate by calculating the crank angles at which the MFB reaches a particular value [59].

Pearson Correlation Coefficient (***CC***)**:** to measure the linear correlation between two sets of data, the Pearson correlation coefficient is also calculated by using the Equation (12). The value for the correlation coefficient ranges from −1 to +1. A value of 1 indicates that there is a perfect linear relationship exists in between the two variables. If the value is 0, it means that there is no linear relationship exists in between the two variables. The slop of the regression determines the sign of the correlation coefficient: positive sign implies that when one variable increases, the other variable also increases, negative sign indicates that when one variable increases, the other variable decreases.

$$CC = \frac{covariance\ (a, b)}{\sigma_a \sigma_b} \tag{12}$$

Where: a and b, represent the two variables, σ_a and σ_b are the standard deviation of the variables a and b. The nominator represents the *covariance* of the two variables, can be calculated from the Equation (13).

$$covariance\ (a, b) = \frac{\sum (a_i - \overline{a})(b_i - \overline{b})}{N - 1} \tag{13}$$

Where: a_i and b_i are the data values for a and b variables, $\overline{a}$ and $\overline{b}$ are mean values for variables a and b, and N is the number of data values.

4. Results and discussions

4.1. Pressure versus crank angle

In order to demonstrate the pressure variations during each cycle, pressure for all the 100 consecutive cycles along with the COV_P curve against each crank angle for a single operating condition are plotted in figures from Figs. 2–5. The pressure variations during each cycle along with COV_P against each crank angle are depicted in Fig. 2. It can be seen from Fig. 2 (a), how pressure varies during each cycle for a complete rotation and Fig. 2 (b) presents a zoom-in figure from −100 to +100 CAD.

It can be observed in Fig. 2 (a) and Fig. 2 (b) that pressure exhibits significant variations during the combustion process and minor variations during non-combustion processes. Furthermore, it can be seen in Fig. 2 (c) that when the inlet valve is closed, pressure begins to increase while COV_P decreases. This decrease in the pressure variations is further confirmed by the plot of log P versus log V/Vmax presented in Fig. 2 (d). In the period from the inlet valve close till the start of combustion, pressure exhibits the least variations as shown in a grey shaded area in Fig. 2 (d).

This decrease in COV_P after IVC can be explained by the definition of COV_P as shown in Fig. 4. The COV_P is calculated by dividing the variation in pressure (numerator) by the average pressure (denominator) for a given crank angle. After IVC until SOC, the numerator mainly reflects small variations in the intake system due to cold flow effects. These variations are relatively minor compared to the significant pressure fluctuations introduced by combustion events. As a result, the COV_P decreases because the denominator, which represents the average compression pressure, is increasing, as depicted in Fig. 4 (a). After EOC similar trend occurs as shown in Fig. 4 (b). The numerator consists of relatively constant pressure differences introduced by previous combustion events, while the denominator decreases due to expansion. This leads to a continuous increase in the ratio from EOC. During the actual combustion event from SOC to EOC, the COV_P can be explained by considering the magnitude of disturbances in the numerator compared to the average pressure during the central phase of combustion.

Secondly, the decrease in COV_P after IVC can be explained by the stabilizing influence of wall heat losses in that phase. Slight variations in the initial conditions for temperature and pressure are amplified during the compression process. While an isotropic compression would preserve the relative variations (COV_P constant), a diabat compression however will reduce them as can be seen in Fig. 2 (c) (decrease of COV_P). Wall heat losses will affect high pressure/temperature cycles more due to a higher temperature gradient which results in lower pressure/temperature progressions. As a result, during the compression process the wall heat losses will lead to a more uniform temperature and pressure curve which results in the COV_P-minimum right before the start of combustion.

***COV_P* curve insights:** The mean pressure curve along with the COV_P against crank angle are presented in Fig. 4. The mean pressure and COV_P curves during one complete crank rotation and zoom-in between −100 and +100 CAD are shown in Fig. 4 (a) and Fig. 4 (b), respectively. The COV_P first shows a plateau of about 3–5% till −200 CAD as presented in Fig. 4 (a). Afterward, when the inlet valve is closed, COV_P curve begins to decrease and reaches its minimum value labeled as first minima, as shown Fig. 4 (b). Then, COV_P curve starts increasing and achieves its maximum value labeled as global maxima in Fig. 4 (b). After that, COV_P curve begins to decline again and forms a second local minimum shown as second the local minima in Fig. 4 (b). It is evident from Fig. 4 that COV_P curve depicts three important points: global minima, global maxima, and second local minima.

The study [50] suggested that the global minima, global maxima, and second local minima can be referred to as SOC, MFB50, and EOC, respectively. These points are labeled in Fig. 4 (b). In order to verify this for an H2-ICE, the heat release was calculated first, and criteria were

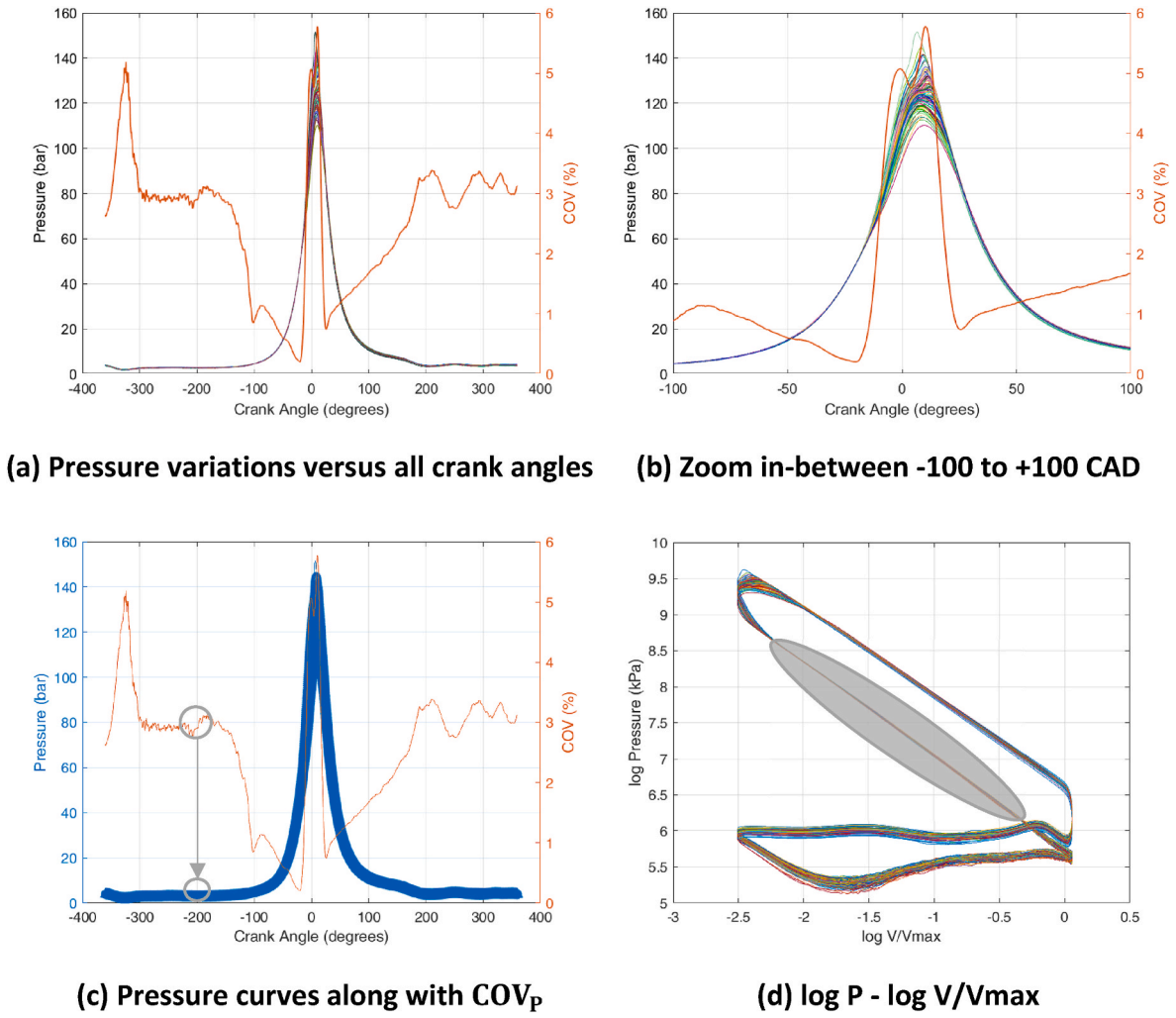

Fig. 2. Pressure variations during each cycle.

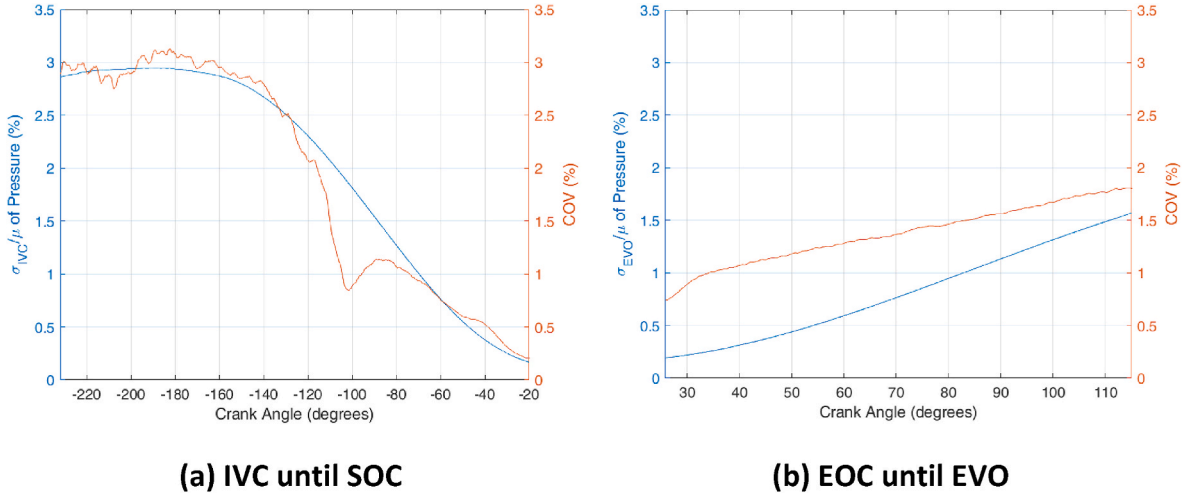

Fig. 3. Ratio of σ_P to μ_P and COV_P versus crank angle.

then established for detecting EOC and SOC.

Heat Release: The apparent heat release, heat loss to the wall, and total heat release were calculated for each operating point using the procedure explained in the previous section. The mean curves of instantaneous heat release rates (HR_A) at each crank angle, and their respective cumulative heat release for each operating point are shown in Fig. 5 (a) and Fig. 5 (b), respectively.

It can be observed from Fig. 5 (a) that the heat release curves do not return to the same levels as before SOC, this is due to a small measurement error caused by a thermal drift of the pressure sensor. The

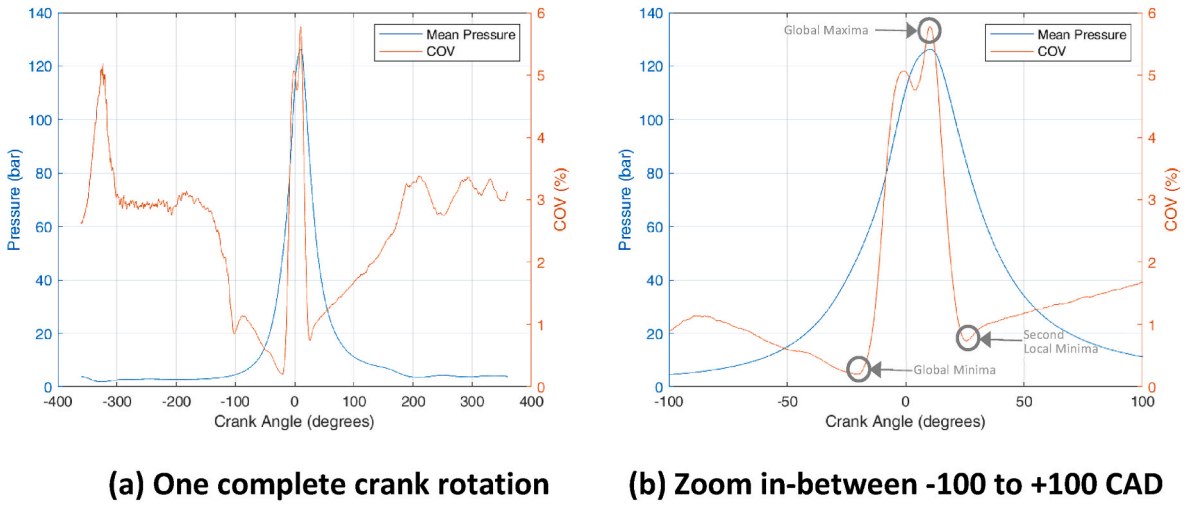

Fig. 4. Mean pressure curve and COV_P versus crank angle.

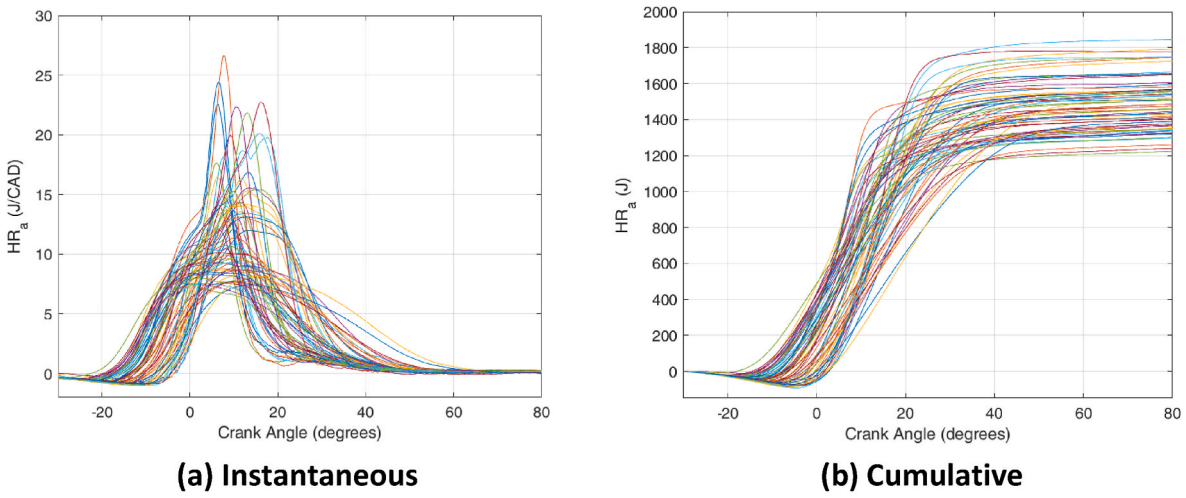

Fig. 5. Mean curves of apparent heat release (HR_A) for each operating condition.

membrane of the piezoelectric sensor is impacted by a thermal wave of the combustion, which causes a slight shift in the voltage signal, resulting in higher heat release rates.

Fig. 5 (a) and Fig. 5 (b) depict the mean cycle-averaged instantaneous (a) and cumulative (b) heat release curves for each operating condition (varied in terms of SA, lambda, boost pressure, EGR), each one denoted by a specific color. It can be observed from Fig. 5 (a) that before reaching its maximum, the curve first approaches a second local maximum. This typical trend is attributed to the piston position and the shape of the combustion chamber. The behavior of the heat release curve along with the corresponding flame-propagation phases is illustrated in Fig. 6.

By using the Woshni equation as explained in the previous section, the heat loss to the walls (Q_W) at each operating point were calculated. The mean curves of instantaneous heat loss to the walls (Q_W) at each crank angle, and their respective cumulative heat release for each operating point are shown in Fig. 7.

By combining the apparent heat release (HR_A) and heat loss to walls (Q_W), the total heat release was calculated. The mean curves of instantaneous total heat release (HR_T) at each crank angle, and their respective cumulative heat release for each operating point are shown in Fig. 8.

Criteria for detecting SOC and EOC: By analyzing the total heat release curves, SOC was selected when the derivate of cumulative total heat release with respect to crank angle is greater than zero. When the derivative of cumulative heat release with respect to crank angle is zero or greater than zero, it indicates the point where the instantaneous heat release curve begins to increase. On the other hand, EOC was considered when instantaneous heat release was less than 0.4 J/CAD.

Based on this criterion for SOC and EOC, results are presented in Figs. 9–11. The SOC and EOC points for all the operating conditions are shown in Fig. 9 (a) and Fig. 9 (b), respectively. The change in the SOC shown in Fig. 9 (a) is mainly due to variation in the SA as SA greatly influence the SOC. It can be noticed that these heat release curves are the mean curves obtained at each operating point. As a result, the SOC and EOC points shown also represent the mean values for each operating condition. By using these SOC and EOC points, the total instantaneous heat release curves were also calculated from SOC to EOC for all the operating conditions and presented in Fig. 10 (b).

After calculating the SOC and EOC based on the mean heat release curves, they are compared with the global minima and second local minima of COV_P curve, respectively. The results of all the operating points are presented in Fig. 11. For a better demonstration, these results are also depicted on a bisector plot shown in Fig. 11 (b). The SOC is found to be more sensitive to the COV_P, because the change in pressure can be detected earlier from the pressure rather than the heat release curve based on the SOC criteria defined above. The EOC is also a little bit late detected from the HR based on the EOC criteria defined above as compared to the COV_P.

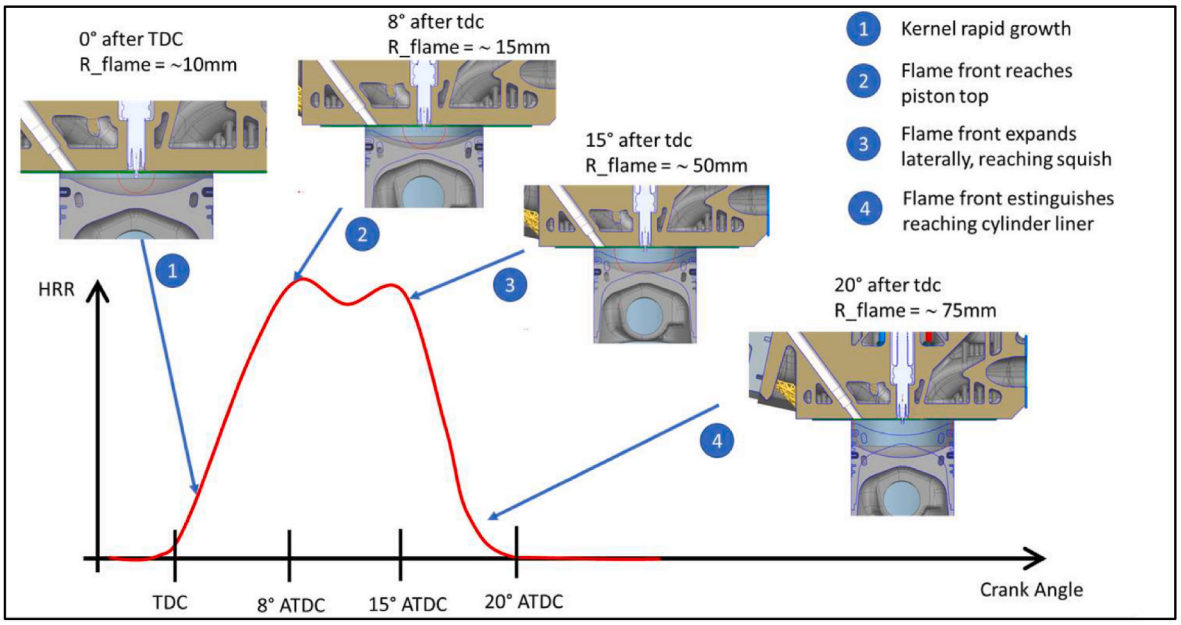

Fig. 6. Heat release curve along with the corresponding flame-propagation phases [60].

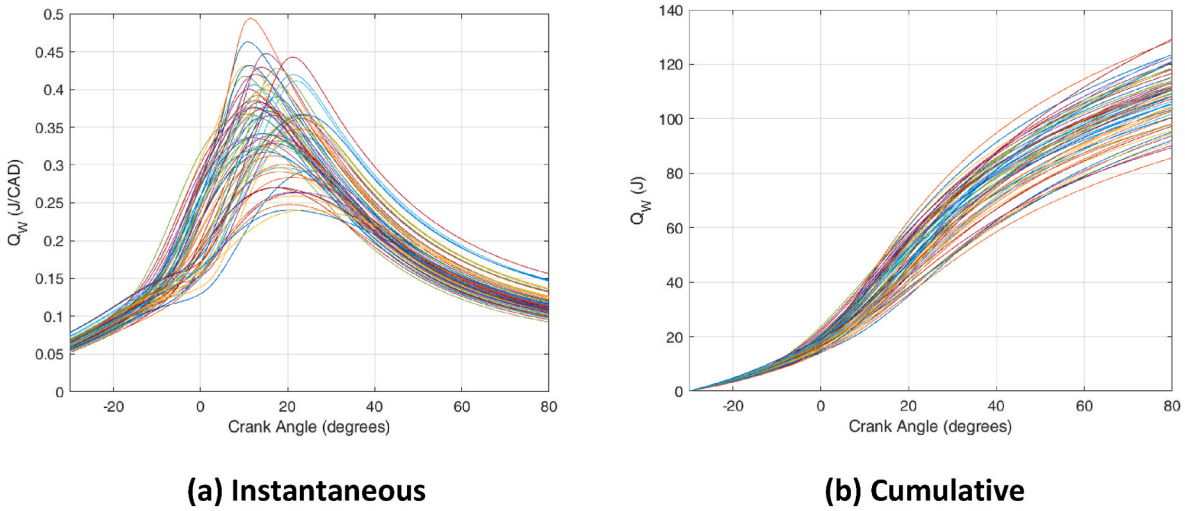

Fig. 7. Mean curves of heat loss to the walls (Q_W) for each operating condition.

It can be seen that the criteria for detecting the EOC is not robust, as a constant value of heat release rate is more likely not to be fit with multiple operating points. Therefore, in this article another criteria for detecting SOC and EOC is also adopted. In the study [45], mass fraction burned criteria for detecting the SOC and EOC is described, the SOC can be considered when 10% of the cumulative mass fraction is burned and EOC can be considered when 90% of the cumulative mass fraction is burned. However, it also mentioned that these numbers are arbitrary and sometimes can be 5% and 95% or even 1% and 99% - depending on the individual problem.

Applying the cumulative mass fraction criteria for detecting the SOC and EOC and the results are presented in Figs. 12–14. In these figures, SOC was selected when 1% of the cumulative mass fraction is burned and EOC was selected when 95% of the cumulative mass fraction is burned. The heat release curves and comparison with the COV_P curve are shown in Figs. 13 and 14, respectively.

It can be seen from Fig. 13 (b) that when the gradient of the heat release curves approach zero the EOC is detected, however, the SOC is detected a little be late as many curves appear to be trimmed. It is evident from Fig. 14 that most of the EOC points are now within the ±5 CAD limit and EOC is a little far from the COV_P curve minima.

Based on the above discussion, in order to achieve the most robust evaluation, a hybrid criterion is recommended. Therefore, selecting the SOC when the derivate of cumulative total heat release with respect to crank angle is greater than zero and EOC when 95% of the cumulative mass fraction is burned. The SOC and EOC points based on this hybrid criterion for each operating condition are presented in Fig. 15. By using this hybrid criterion, the total instantaneous and cumulative heat release curves were calculated from SOC to EOC for all the operating conditions and presented in Fig. 16.

All the further calculations and results in this article are based on the mean heat release curves from SOC to EOC, as shown in Fig. 16.

Fifty percent mass fraction burned (MFB50): Based on the mean curves of cumulative total heat release shown in Fig. 16 (b), mass fraction burned values for all the operating conditions were calculated. The cumulative heat at the EOC was considered as reaching 100% of the mass fraction burned. Hence, the crank angle at which half of this cumulative heat is released is referred to as MFB50. The crank angles at

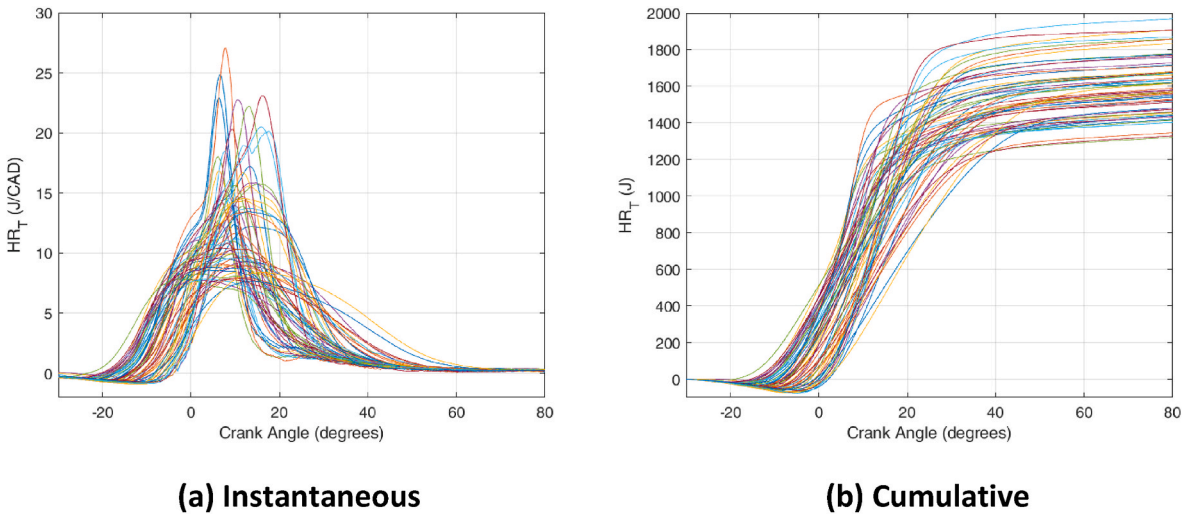

Fig. 8. Mean curves of total heat release (HR_T) for each operating condition.

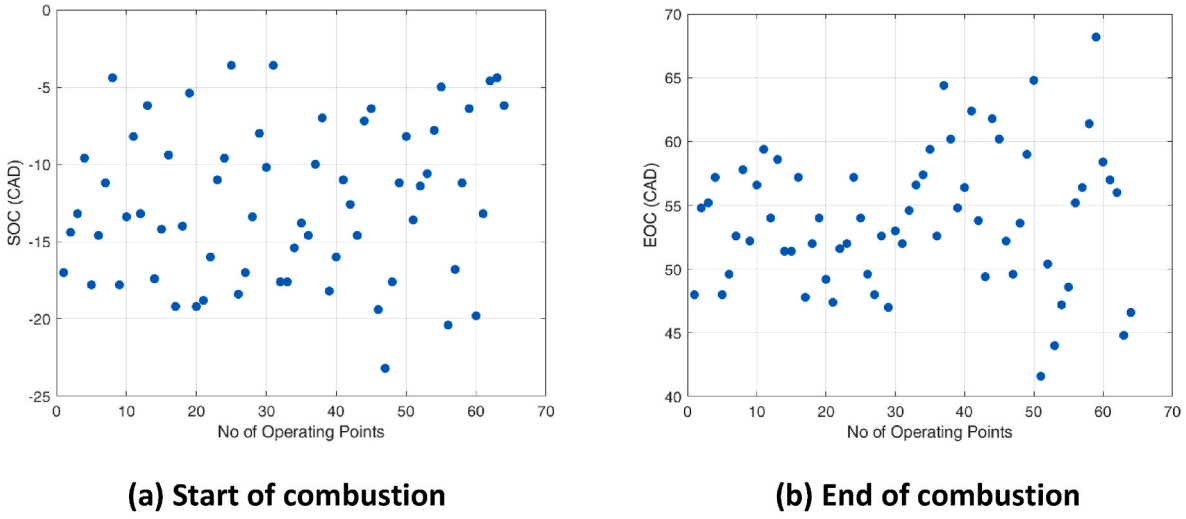

Fig. 9. Crank angle in degrees for all the operating conditions.

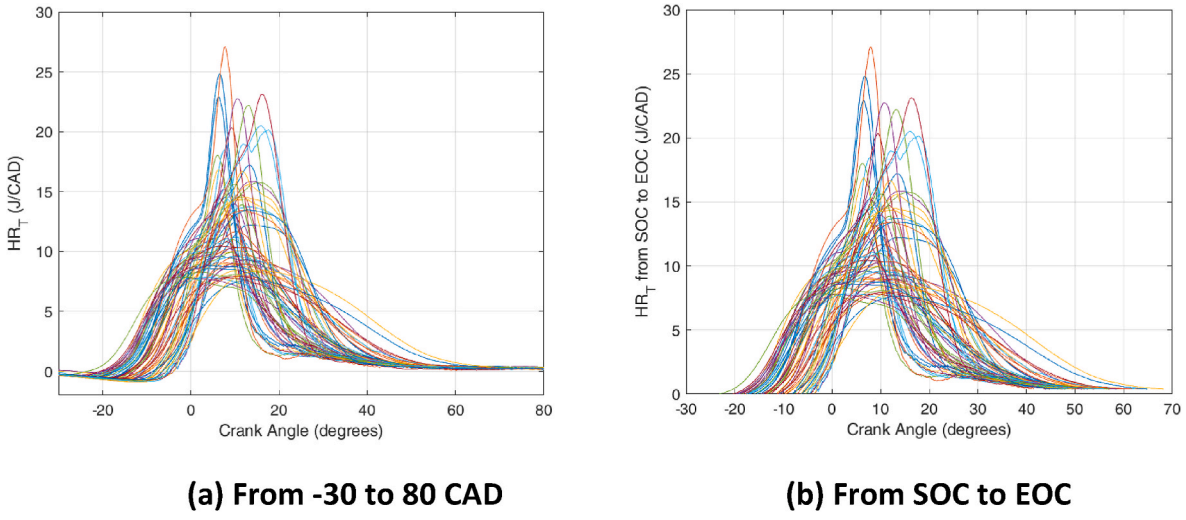

Fig. 10. Mean curves of total heat release (HR_T) for each operating condition.

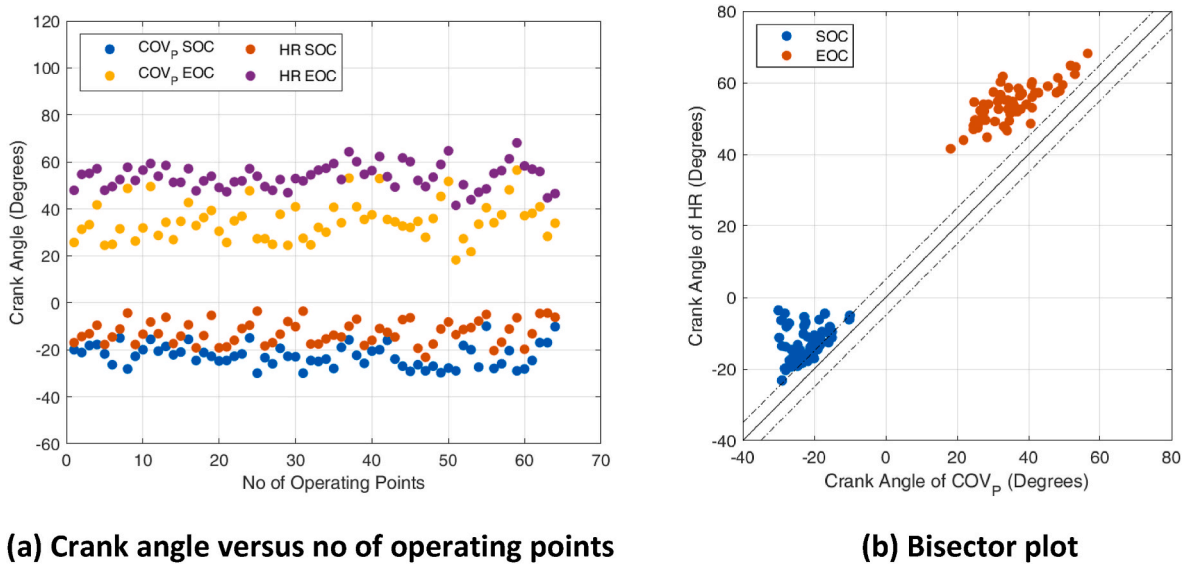

Fig. 11. Comparison of SOC and EOC based on COV and HR.

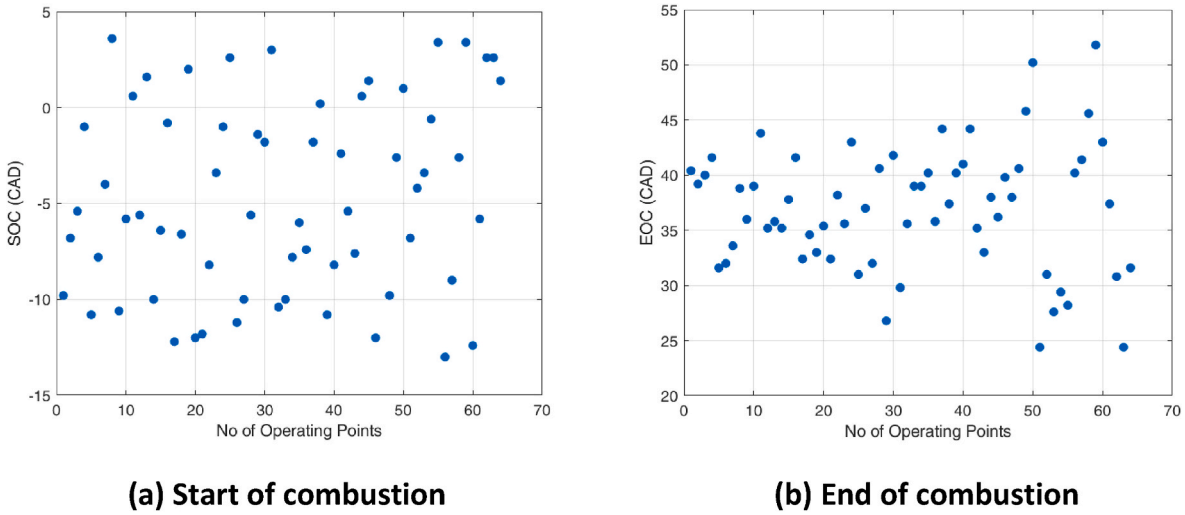

Fig. 12. Crank angle in degrees for all the operating conditions.

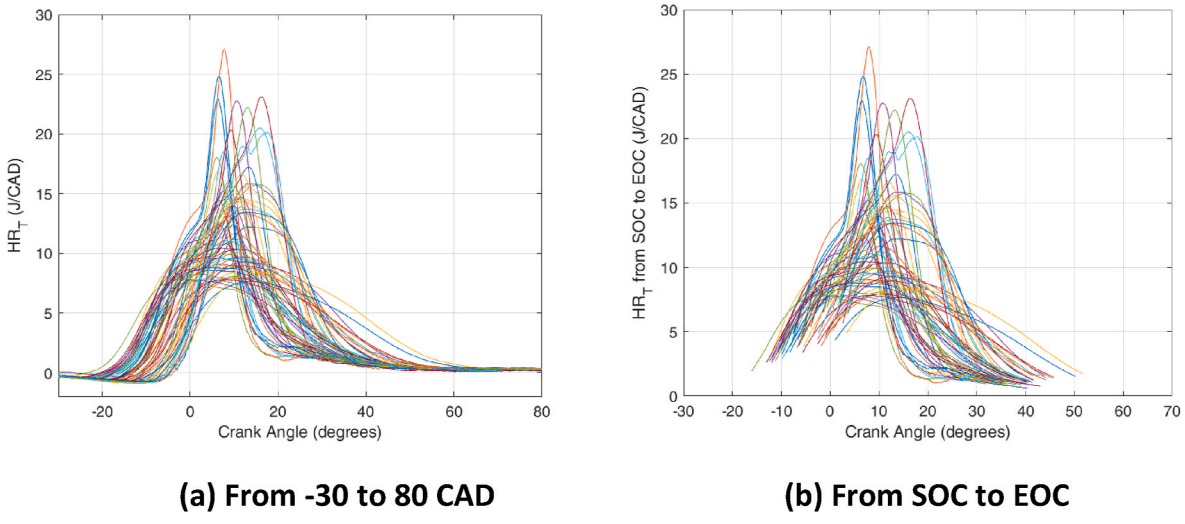

Fig. 13. Mean curves of total heat release (HR_T) for each operating condition.

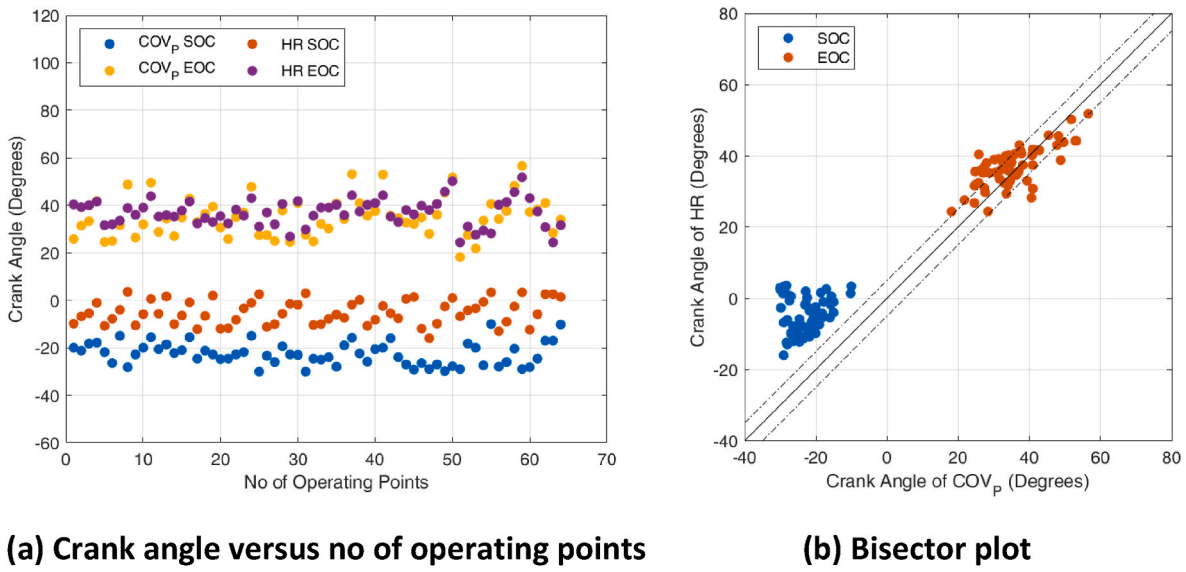

Fig. 14. Comparison of SOC and EOC based on COV and HR.

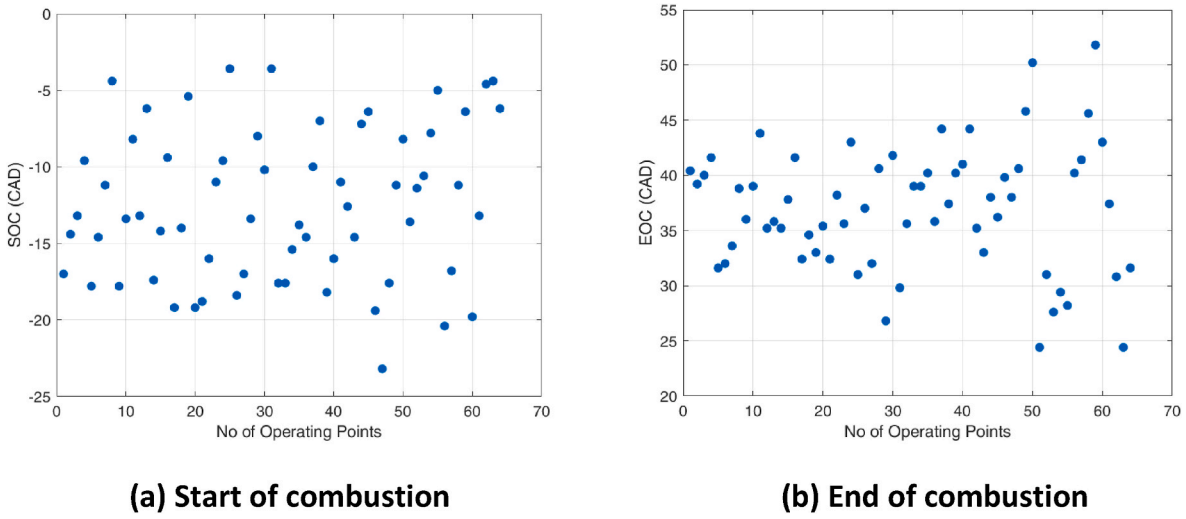

Fig. 15. Crank angle in degrees for all the operating conditions.

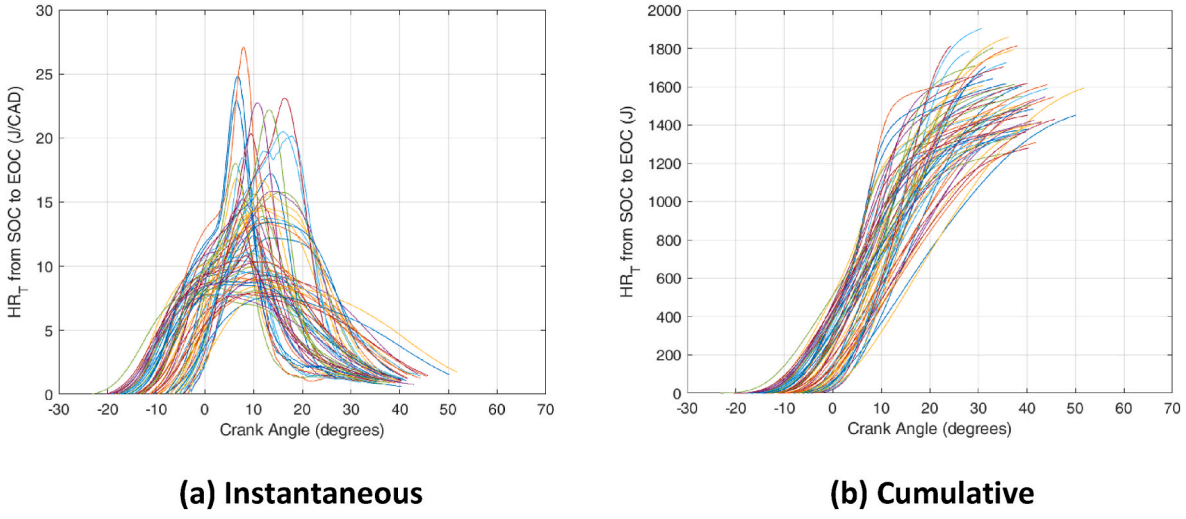

Fig. 16. Mean curves of total heat release (HR_T) from SOC to EOC for each operating condition.

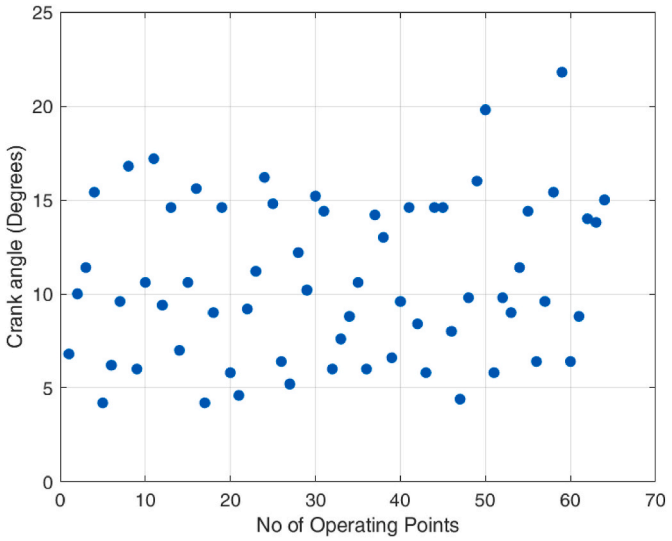

Fig. 17. Crank angle of MFB50 for each operating condition.

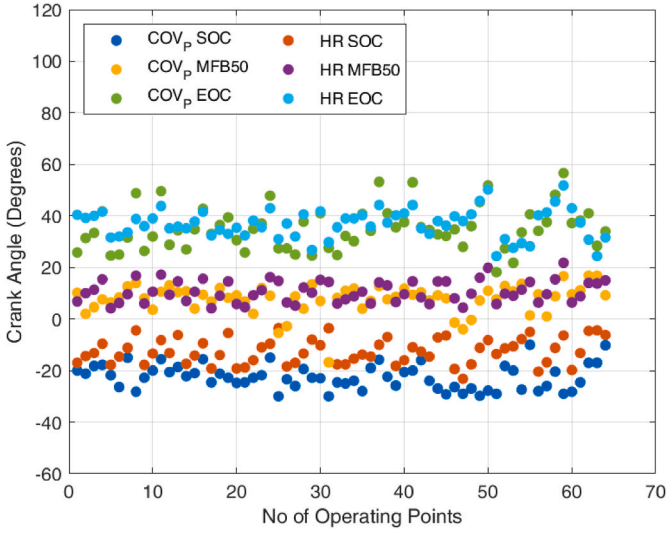

Fig. 18. Comparison of SOC, MFB50, and EOC based on COV_P and HR.

which MFB50 occur for all the operating conditions are presented in Fig. 17.

After calculating the SOC, MFB50, and EOC based on the mean heat release curves, they are compared with the global minima, global maxima, and second local minima of COV_P curve, respectively. The results of all the operating points are presented in Fig. 18. For a better demonstration, these results are also depicted on a bisector plot shown in Fig. 19.

From Figs. 18 and 19, most of the points for MFB50 and EOC correspond to the COV_P global maxima and COV_P minima, respectively. It is evident from Fig. 19 that the majority points for MFB50 and EOC are within ±5 CAD; however, SOC is found to be more sensitive to COV_P, because changes in pressure can be detected earlier from the pressure signal rather than the heat release. It can be said that COV_P is a better parameter for measuring cycle-by-cycle variations because COV_P is based on the mean and standard deviation at each crank angle, whereas heat release is calculated using only the mean pressure for each operating condition.

PFP and COV_P at PFP: To evaluate the cycle-by-cycle variations, the COV_P at the crank angle where PFP occurs is also calculated for all the operating conditions. The peak firing pressure versus the crank angle at

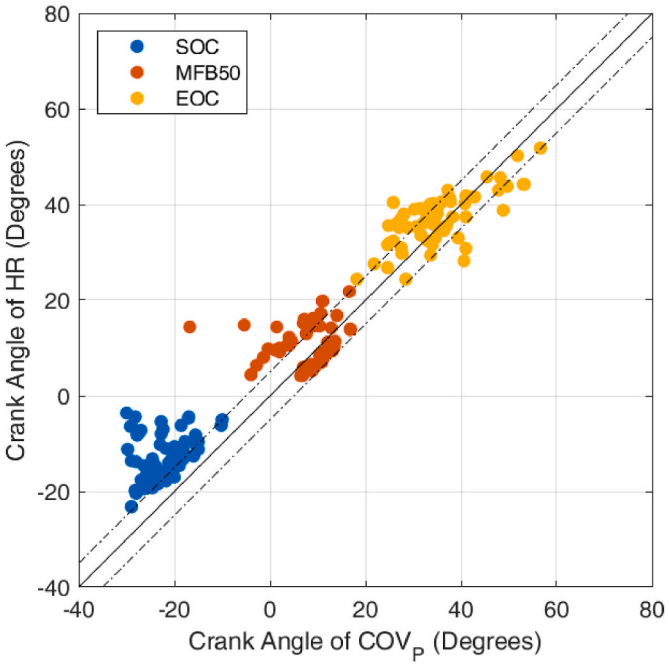

Fig. 19. Bisector plot for comparing SOC, MFB50, and EOC points between COV_P and HR.

which PFP occurs is presented in Fig. 20 (a) and the COV_P at PFP versus the PFP is presented in Fig. 20 (b).

It is evident from Fig. 20 (a) that as the crank angle at which PFP occurs increases, the PFP decreases with a relatively weak correlation value of −0.26. Fig. 20 (b) demonstrates that an increase in PFP results in higher COV_P at PFP with a relatively weak correlation value of 0.22.

Further, the crank angle at which peak firing pressure occurs is also compared with MFB50 and global maxima of COV_P curve. The comparison of PFP with MFB50 based on mean heat release curves and global maxima of COV_P curve is presented in Fig. 21. For a better demonstration, these results are also presented on a bisector plot shown in Fig. 22 with PFP on the x-axis. Bisector lines and accuracy lines with a ±5 CAD are also shown in Fig. 22.

It can be concluded from Figs. 21 and 22 that for most of the operating points, the crank angle of PFP corresponds to the crank angle of MFB50 as well as the crank angle of COV_P global maxima. However, there are some operating points in which the crank angle of PFP does not correspond to the crank angles of MFB50 and COV_P global maxima. The results are also confirmed by changing the x-axis and there is no difference in the results, therefore, it can be concluded that results are independent of the axis.

Indicated mean effective pressure (IMEP): The indicated mean effective pressure (IMEP) for all operating conditions was also calculated in the article. The IMEP for all the operating conditions is plotted in Fig. 23.

Fig. 23 (a) shows a typical and as expected trend that an increase in the crank angle of the PFP results in an increase in IMEP with a correlation coefficient of 0.68 which indicates a strong positive linear relationship. Fig. 23 (b) concludes that as the IMEP increases, the COV_{IMEP} also increases with a relatively weak linear relationship as the correlation coefficient is 0.3. Of course, the increase in the COV_{IMEP} is mainly due to the sweep of operating parameters like lambda, boost pressure, and spark advance, which are not plotted in Fig. 23 (b). The value of 3% for COV_{IMEP} is considered as an acceptable in industrial applications; however, lower values are preferable for smoother and more efficient engine operation. For the state of the art in automotive industry, the value of COV_{IMEP} should be less than 1%.

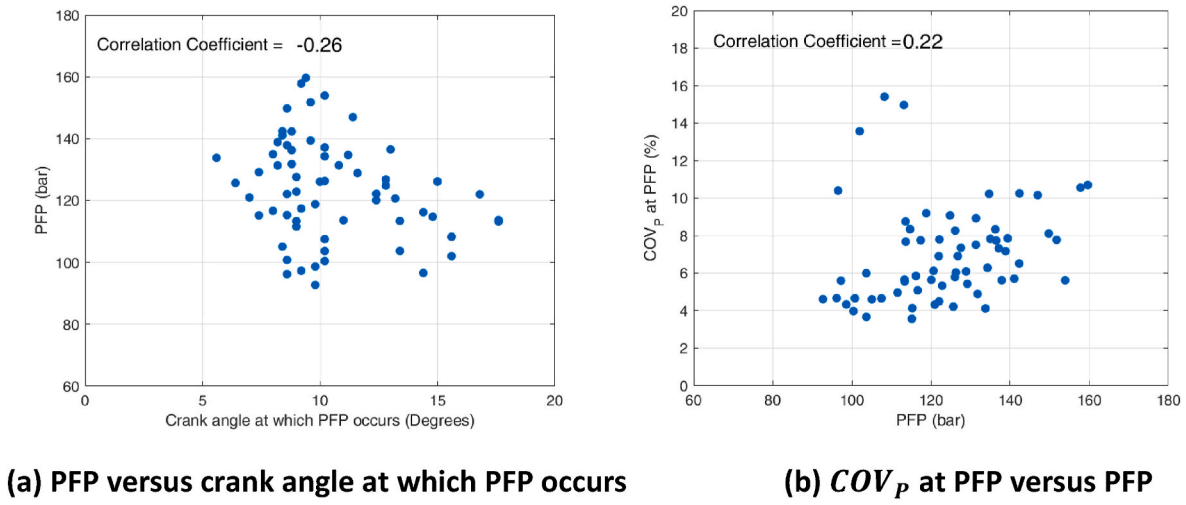

Fig. 20. Peak firing pressure.

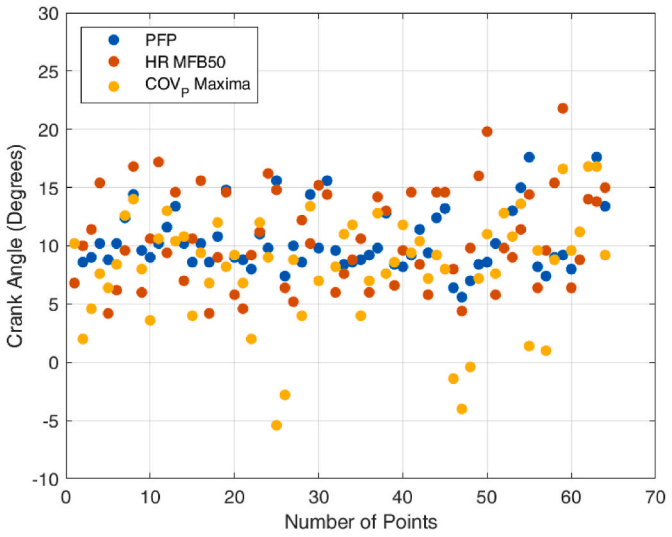

Fig. 21. Comparison between PFP, MFB50 based on heat release curve and global maxima of COV_P.

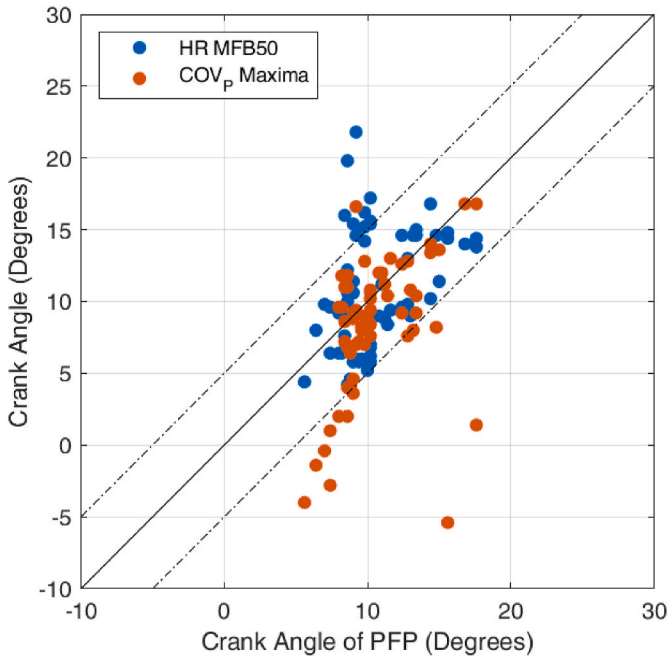

Fig. 22. Bisector plot comparing PFP, HR MFB50, and global maxima of COV_P with PFP on the x-axis.

It can be observed that the IMEP has a single value for one cycle on each operating condition, and only one COV_{IMEP} can be calculated for all the tested cycles in that operating condition. However, the COV_P has values against each crank angle, resulting in COV_P values for each crank angle across all the tested cycles in a single operating condition.

4.2. Effects of SA in SI H2-ICE

The COV_P curve is analyzed in detail by varying the spark advance. The ignition delay, first and second-half combustion, and combustion duration along with their correlation coefficients and trendlines are presented in Fig. 24. The correlation coefficients with respect to spark advance are also tabulated in Table 4.

It can be seen from Fig. 24 that with the increase of SA, the ignition delay is decreased meaning that as the spark advances, the combustion starts earlier which results in the decrease of ignition delay. The correlation coefficient between ignition delay and SA is −0.65 which indicates a relatively strong negative linear relationship between them. Total combustion duration is not convergent, as the correlation coefficient between combustion duration and SA is only −0.1, some of the points of increased SA show slower combustion, and some of the increased SA also show faster combustion.

As shown in Fig. 24 that the points for the second half combustion are dispersed with a correlation coefficient of 0.02 although the trend line is towards increasing. However, the points for the first half are not as dispersed as compared to the second half, along with a strong correlation coefficient value of 0.65, indicating that the second half is much more likely to be affected by changing SA and change in combustion duration is mainly due to the change in the second half. Since the combustion duration decreases with the increase of SA, it indicates that the efficiency increases and the change in combustion duration is mainly regulated by second half combustion.

4.3. Effects of equivalence ratio in SI H2-ICE

The effects of equivalence ratio on ignition delay and combustion duration including first and second half combustion are presented in Fig. 25. The correlation coefficients with respect to the equivalence ratio

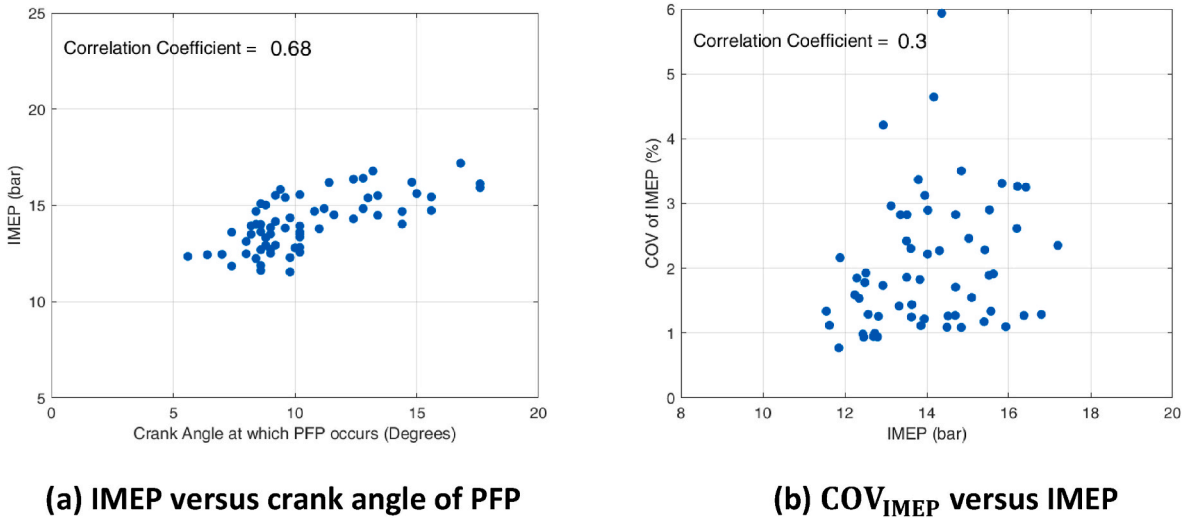

Fig. 23. Indicated mean effective pressure for all operating conditions.

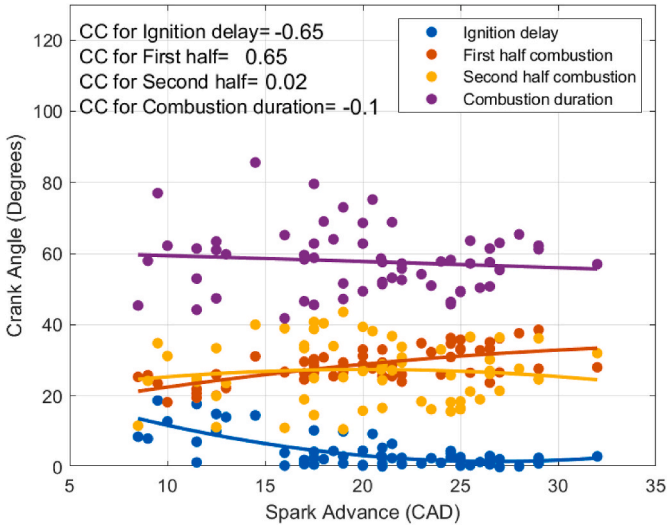

Fig. 24. Effects of Spark Advance with correlation coefficients and trendlines.

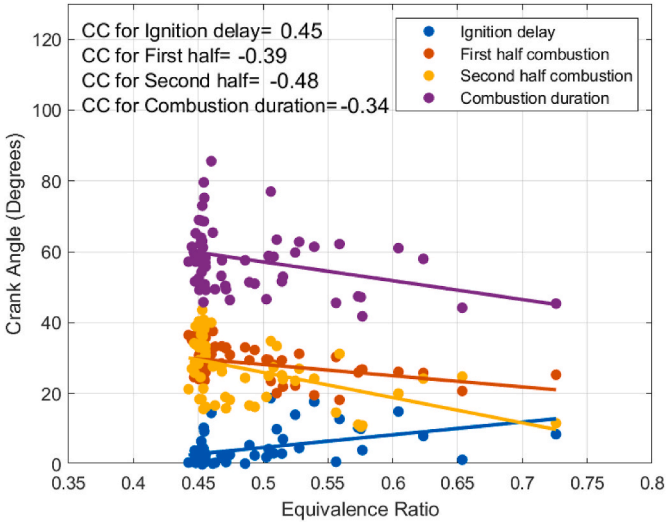

Fig. 25. Effects of Equivalence Ratio with correlation coefficients and trendlines.

Table 4
Correlation coefficients between Spark Advance.

Ignition delay versus SA	−0.65
First-half combustion versus SA	0.65
Second-half combustion versus SA	0.02
Combustion duration versus SA	−0.1

Table 5
Correlation coefficients between Equivalence Ratio.

Ignition delay versus equivalence ratio	0.45
First-half combustion versus equivalence ratio	−0.39
Second-half combustion versus equivalence ratio	−0.48
Combustion duration versus equivalence ratio	−0.34

are shown in Fig. 25 as well as tabulated in Table 5.

Fig. 25 shows the combustion duration versus the equivalence ratio (in the range 0.45–0.65). Due to the increase of the laminar flame speed with the equivalence ratio the combustion duration decreases, as expected, with a coefficient value of −0.34 (see Table 5 and Fig. 25) indicating a relatively weak relationship [61].

However, the ignition delay increases, as the equivalence ratio increases, with a correlation coefficient of 0.45, indicating a relatively weak positive relationship. One of the possible reasons is that the mixture is becoming richer, resulting in a change in reaction kinetics that leads to a delay in the initiation of the combustion reaction. Alternatively, it may also be possible that there is more heat absorption, resulting in a lower mixture temperature, which, in turn, leads to an increase in ignition delay.

4.4. Effects of Volumetric Efficiency in SI H2-ICE

The ignition delay, first-half combustion, second-half combustion, and combustion duration were also analyzed by varying volumetric efficiency. The results with correlation coefficients and trendlines are shown in Fig. 26. The correlation coefficients with respect to volumetric efficiency are also shown in Table 6.

The volumetric efficiency is a measure of how much volume of air-fuel ratio can be drawn into the combustion chamber. High volumetric efficiency means a higher volume of air-fuel ratio and that will lead to enhanced combustion. In general, enhanced combustion means

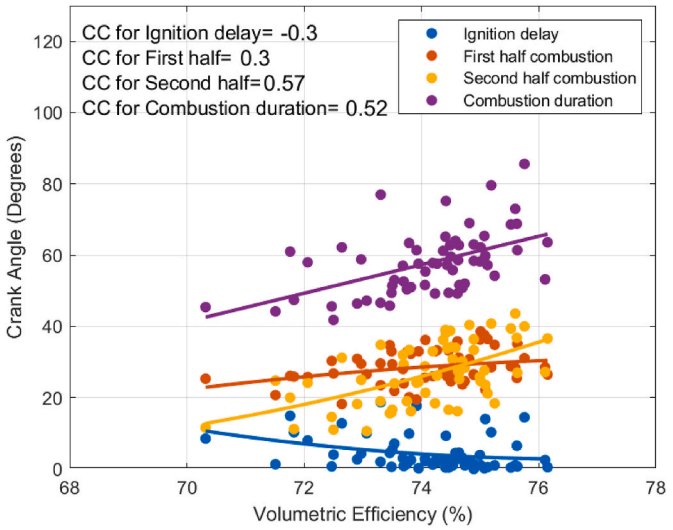

Fig. 26. Effects of Volumetric Efficiency with correlation coefficients and trendlines.

Table 6
Correlation coefficients between Volumetric Efficiency.

Ignition delay versus volumetric efficiency	−0.3
First-half combustion versus volumetric efficiency	0.3
Second-half combustion versus volumetric efficiency	0.57
Combustion duration versus volumetric efficiency	0.52

shorter combustion duration and a high percentage of fuel burnt.

With the increase in volumetric efficiency, combustion duration increases with a correlation coefficient of 0.52, rather than decreasing. It may be due to the leaner air-fuel mixture as the lean mixture takes longer to burn as compared to the richer mixture. Or it could be due to the ignition timing because the variations in volumetric efficiency can affect the optimal ignition timing.

However, if we look into the ignition delay results as shown in Fig. 26, it is decreased with the increase in volumetric efficiency, it seems more logical and it can contribute to the improvement of the H2-ICE. As the volumetric efficiency is increased, the higher volume of air-fuel ratio is drawn to the combustion chamber resulting in a decrease in the actual SOC.

5. Conclusions

An experimental study of cycle-by-cycle variations was performed in a hydrogen spark ignition internal combustion engine. Based on the above discussions and results, the following conclusions are made:

1. Pressure exhibits significant variations during the combustion process and minor variations during non-combustion processes. In the period from the inlet valve close till the start of combustion, pressure exhibits the least variations. COV_P curve depicts three important points in H2-ICE as well: global minima, global maxima, and second local minima.
2. The magnitude of the COV_P curve changes across all the operating conditions, however, the shape of the COV_P curve remains unchanged across all the operating conditions, indicating its independence from the operating condition in an H2-ICE.
3. A hybrid criterion for determining the SOC and EOC is proposed: SOC can be considered when the derivate of cumulative total heat release with respect to crank angle is greater than zero and EOC can be detected based the cumulative mass fraction burned.
4. The comparison of the COV_P curve with the heat release curve revealed that the COV_P global maxima and COV_P second local minima are phased with MFB50 and EOC, respectively. The SOC detection through COV_P is found to be more sensitive rather than the heat release curve, because the change in pressure can be revealed earlier from the pressure rather than the heat release.
5. It can be said that COV_P is a better parameter for measuring cycle-by-cycle variations because it is based on the mean and standard deviation at each crank angle, whereas heat release is calculated using only the mean pressure for each operating condition.
6. It was assessed that, generally, the crank angle of PFP corresponds to the crank angle of MFB50 as well as the crank angle of COV_P global maxima. However, there are some operating points in which the crank angle of PFP does not correspond to the crank angles of MFB50 and COV_P global maxima.
7. The spark advance sweep revealed that with the increase of SA, the ignition delay is decreased with a correlation coefficient of −0.65 which indicates a relatively strong negative linear relationship between them. The points for the first half are not much as dispersed as compared to the second half, along with a strong correlation coefficient value of 0.65, indicating that the second half is much more likely to be affected by changing SA.

The presented work provides a different methodology for a fast combustion analysis of hydrogen engines. The presented cylinder pressure cycle-by-cycle analysis allows fast and accurate detection of the main combustion features (start of combustion, center of combustion, end of combustion and operation condition stability) without the use of more complex procedures like the rate of heat release analysis. By the way, furthermore, such procedures could be implemented in the engine control unit for the automatic control of cycle-by-cycle variations enhancing the efficiency of the engine.

Funding

Naqash Azeem received funding through grant no. DOT1341429 from the Ministry of University and Research, Italy, within the funding program PON R&I 2014–2020, Asse I "Investimenti in Capitale Umano'' Azione I.1 "Dottorati Innovativi con caratterizzazione industriale''.

Declaration of competing interest

The authors declare that they have no known competing financial interests or personal relationships that could have appeared to influence the work reported in this paper.

Appendix A. Supplementary data

Supplementary data to this article can be found online at https://doi.org/10.1016/j.ijhydene.2024.02.182.

References

[1] Nicoletti G, Arcuri N, Nicoletti G, Bruno R. A technical and environmental comparison between hydrogen and some fossil fuels. Energy Convers Manag 2015; 89:205–13. https://doi.org/10.1016/j.enconman.2014.09.057.
[2] Revankar ST. Chapter four - nuclear hydrogen production. Academic Press Storage and Hybridization of Nuclear Energy; 2019. https://doi.org/10.1016/B978-0-12-813975-2.00004-1. 49-117.
[3] Dincer I, Acar C. Review and evaluation of hydrogen production methods for better sustainability. Int J Hydrogen Energy 2015;40(34):11094–111. https://doi.org/10.1016/j.ijhydene.2014.12.035.
[4] Chaubey R, Sahu S, James OO, Maity S. A review on development of industrial processes and emerging techniques for production of hydrogen from renewable and sustainable sources. Renew Sustain Energy Rev 2013;23:443–62. https://doi.org/10.1016/j.rser.2013.02.019.
[5] Chi J, Yu H. Water electrolysis based on renewable energy for hydrogen production. Chin J Catal 2018;39(3):390–4. https://doi.org/10.1016/S1872-2067(17)62949-8.

[6] Lattin WC, Utgikar VP. Transition to hydrogen economy in the United States: a 2006 status report. Int J Hydrogen Energy 2007;32(15):3230–7. https://doi.org/10.1016/j.ijhydene.2007.02.004.

[7] Elam CC, Padró CEG, Sandrock G, Luzzi A, et al. Realizing the hydrogen future: the International Energy Agency's efforts to advance hydrogen energy technologies. Int J Hydrogen Energy 2003;28(6):601–7. https://doi.org/10.1016/S0360-3199(02)00147-7.

[8] Veziroğlu TN, Şahi S. 21st Century's energy: hydrogen energy system. Energy Convers Manag 2008;49(7):1820–31. https://doi.org/10.1016/j.enconman.2007.08.015.

[9] Dunn S. Hydrogen futures: toward a sustainable energy system. Int J Hydrogen Energy 2002;27(3):235–64. https://doi.org/10.1016/S0360-3199(01)00131-8.

[10] Bose T, Malbrunot P. Hydrogen: facing the energy challenges of the 21st century. John Libbey Eurotext; 2007.

[11] Árnason B, Sigfússon TI. Iceland — a future hydrogen economy. Int J Hydrogen Energy 2000;25(5):389–94. https://doi.org/10.1016/S0360-3199(99)00077-4.

[12] Verhelst S. Recent progress in the use of hydrogen as a fuel for internal combustion engines. Int J Hydrogen Energy 2014;39(2):1071–85. https://doi.org/10.1016/j.ijhydene.2013.10.102.

[13] White CM, Steeper RR, Lutz AE. The hydrogen-fueled internal combustion engine: a technical review. Int J Hydrogen Energy 2006;31(10):1292–305. https://doi.org/10.1016/j.ijhydene.2005.12.001.

[14] Azeem N, Beatrice C, Vassallo A, Pesce F, et al. Review and Assessment of the Material's Compatibility for Rubbers and Elastomers in Hydrogen Internal Combustion Engines. SAE Technical Paper 2022-01-0331. 2022. https://doi.org/10.4271/2022-01-0331.

[15] Azeem N, Beatrice C, Vassallo A, Pesce F, et al. Review and evaluation of metals and alloy's compatibility with hydrogen-fueled internal combustion engines. Int J Engine Res 2023;24(9):4204–25. https://doi.org/10.1177/14680874231184981.

[16] Azeem N, Beatrice C, Vassallo A, Pesce F, et al. Comparative Analysis of Different Methodologies to Calculate Lambda (Λ) Based on Extensive and Systemic Experimentation on a Hydrogen Internal Combustion Engine. SAE Technical Paper 2023-01-0340. 2023. https://doi.org/10.4271/2023-01-0340.

[17] Hänggi S, Elbert P, Bütler T, Cabalzar U, et al. A review of synthetic fuels for passenger vehicles. Energy Rep 2019;5:555–69. https://doi.org/10.1016/j.egyr.2019.04.007.

[18] von Helmolt R, Eberle U. Fuel cell vehicles: status 2007. J Power Sources 2007;165(2):833–43. https://doi.org/10.1016/j.jpowsour.2006.12.073.

[19] Shelef M, Kukkonen CA. Prospects of hydrogen-fueled vehicles. Prog Energy Combust Sci 1994;20(2):139–48. https://doi.org/10.1016/0360-1285(94)90008-6.

[20] Di Vece G, Di Nunno D, Bilancia M, Verdino V. Development of a Total Cost of Ownership Model to Compare Bevs, Fcevs and Diesel Powertrains on Bus Applications. SAE Technical Paper 2022-37-0030. 2022. https://doi.org/10.4271/2022-37-0030.

[21] Eichlseder H, Wallner T, Freymann R, Ringler J. The Potential of Hydrogen Internal Combustion Engines in a Future Mobility Scenario. SAE Technical Paper 2003-01-2267. 2003. https://doi.org/10.4271/2003-01-2267.

[22] Wimmer A, Wallner T, Ringler J, Gerbig F. H2-Direct Injection–A Highly Promising Combustion Concept. SAE Technical Paper 2005-01-0108. 2005. https://doi.org/10.4271/2005-01-0108.

[23] Verhelst S, Sierens R, Verstraeten S. A critical review of experimental research on hydrogen fueled SI engines. SAE Trans 2006;115:264–74. http://www.jstor.org/stable/44687302.

[24] Verhelst S, Wallner T. Hydrogen-fueled internal combustion engines. Prog Energy Combust Sci 2009;35(6):490–527. https://doi.org/10.1016/j.pecs.2009.08.001.

[25] Kawamura A, Yanai T, Sato Y, Naganuma K, et al. Summary and Progress of the Hydrogen ICE Truck Development Project. SAE Technical Paper 2009-01-1922. 2009. https://doi.org/10.4271/2009-01-1922.

[26] Kawamura A, Sato Y, Naganuma K, Yamane K, et al. Development Project of a Multi-Cylinder DISI Hydrogen ICE System for Heavy Duty Vehicles. SAE Technical Paper 2010-01-2175. 2010. https://doi.org/10.4271/2010-01-2175.

[27] Obermair H, Scarcelli R, Wallner T. Efficiency Improved Combustion System for Hydrogen Direct Injection Operation. SAE Technical Paper 2010-01-2170. 2010. https://doi.org/10.4271/2010-01-2170.

[28] Wallner T, Matthias NS, Scarcelli R, Kwon JC. Evaluation of the efficiency and the drive cycle emissions for a hydrogen direct-injection engine. Proc Inst Mech Eng - Part D J Automob Eng 2013;227(1):99–109. https://doi.org/10.1177/0954407012461875.

[29] Verhelst S, Maesschalck P, Rombaut N, Sierens R. Increasing the power output of hydrogen internal combustion engines by means of supercharging and exhaust gas recirculation. Int J Hydrogen Energy 2009;34(10):4406–12. https://doi.org/10.1016/j.ijhydene.2009.03.037.

[30] Heindl R, Eichlseder H, Spuller C, Gerbig F, et al. New and innovative combustion systems for the H_2–ICE, compression ignition and combined processes. SAE Int J Engines 2009;2(1):1231–50. http://www.jstor.org/stable/26308466.

[31] Welch A, Mumford D, Munshi S, Holbery J, et al. Challenges in Developing Hydrogen Direct Injection Technology for Internal Combustion Engines. SAE Technical Paper 2008-01-2379. 2008. https://doi.org/10.4271/2008-01-2379.

[32] Sopena C, Diéguez PM, Sáinz D, Urroz JC, et al. Conversion of a commercial spark ignition engine to run on hydrogen: performance comparison using hydrogen and gasoline. Int J Hydrogen Energy 2010;35(3):1420–9. https://doi.org/10.1016/j.ijhydene.2009.11.090.

[33] Yamane K. Hydrogen Fueled Ice, Successfully Overcoming Challenges Through High Pressure Direct Injection Technologies: 40 Years of Japanese Hydrogen Ice Research and Development. SAE Technical Paper 2018-01-1145. 2018. https://doi.org/10.4271/2018-01-1145.

[34] Srinivasan C, Subramanian R. Hydrogen as a spark ignition engine fuel technical review. Int J Mech Mechatron Eng IJMME-IJENS 2014;14:111–7.

[35] Dimitriou P, Tsujimura T. A review of hydrogen as a compression ignition engine fuel. Int J Hydrogen Energy 2017;42(38):24470–86. https://doi.org/10.1016/j.ijhydene.2017.07.232.

[36] Kumar V, Gupta D, Kumar N. Hydrogen use in internal combustion engine: a review. Int J Adv Cult Technol 2015;3(2):87–99. https://doi.org/10.17703/IJACT.2015.3.2.87.

[37] Faizal M, Chuah L, Lee C, Hameed A, et al. Review of hydrogen fuel for internal combustion engines. J Mech Eng Res Dev 2019;42(3):36–46. https://doi.org/10.26480/jmerd.03.2019.35.46.

[38] Molnarne M, Schendler T, Schröder V. Explosionsbereiche von Gasgemischen. Wirtschaftsverlag NW; 2008.

[39] Walter L, Sommermann A, Hyna D, Malischewski T, et al. The H2 combustion engine—the forerunner of a zero emissions future. In: Presented at 42nd international Vienna motor symposium; April 2021. p. 29–30.

[40] Boretti A. Transient positive ignition engines have now surpassed the 50% fuel conversion efficiency barrier. Int J Hydrogen Energy 2019;44(14):7051–2. https://doi.org/10.1016/j.ijhydene.2019.01.237.

[41] Ono R, Nifuku M, Fujiwara S, Horiguchi S, et al. Minimum ignition energy of hydrogen–air mixture: effects of humidity and spark duration. J Electrost 2007;65(2):87–93. https://doi.org/10.1016/j.elstat.2006.07.004.

[42] Gandhi RD. Use of hydrogen in internal combustion engine. Int J Eng Tech Res (IJETR) 2015;2(4):207–16.

[43] Ciniviz M, Köse H. Hydrogen use in internal combustion engine: a review. Int J Adv Eng Technol 2012;1(1):1–15.

[44] Duan X, Xu L, Xu L, Jiang P, et al. Performance analysis and comparison of the spark ignition engine fuelled with industrial by-product hydrogen and gasoline. J Clean Prod 2023;424:138899. https://doi.org/10.1016/j.jclepro.2023.138899.

[45] Heywood JB. Internal combustion engine fundamentals. New York: McGraw-Hill; 1988. p. 413–23.

[46] Kalghatgi GT. Spark ignition, early flame development and cyclic variation in I.C. Engines. SAE Trans 1987;96:149–61. http://www.jstor.org/stable/44470832.

[47] Keck JC, Heywood JB, Noske G. Early flame development and burning rates in spark ignition engines and their cyclic variability. SAE Trans 1987;96:162–75. http://www.jstor.org/stable/44470833.

[48] Bates SC. Flame imaging studies of cycle-by-cycle combustion variation in a SI four-stroke engine. SAE Trans 1989;98:2015–41. http://www.jstor.org/stable/44581085.

[49] Ishii K, Sasaki T, Urata Y, Yoshida K, et al. Investigation of cyclic variation of IMEP under lean burn operation in spark-ignition engine. SAE Trans 1997;106:816–24. http://www.jstor.org/stable/44731614.

[50] Zervas E. Correlations between cycle-to-cycle variations and combustion parameters of a spark ignition engine. Appl Therm Eng 2004;24(14–15):2073–81. https://doi.org/10.1016/j.applthermaleng.2004.02.008.

[51] Fischer J, Velji A, Spicher U. Investigation of cycle-to-cycle variations of in-cylinder processes in gasoline direct injection engines operating with variable tumble systems. SAE Trans 2004;113:154–63. http://www.jstor.org/stable/44723497.

[52] Duan X, Deng B, Liu Y, Zou S, et al. An experimental study the impact of the hydrogen enrichment on cycle-to-cycle variations of the large bore and lean burn natural gas spark-ignition engine. Fuel 2020;282:118868. https://doi.org/10.1016/j.fuel.2020.118868.

[53] Heywood JB, Vilchis FR. Comparison of flame development in a spark-ignition engine fueled with propane and hydrogen. Combust Sci Technol 1984;38(5–6):313–24. https://doi.org/10.1080/00102208408923778.

[54] Ma F, Wang Y, Liu H, Li Y, et al. Effects of hydrogen addition on cycle-by-cycle variations in a lean burn natural gas spark-ignition engine. Int J Hydrogen Energy 2008;33(2):823–31. https://doi.org/10.1016/j.ijhydene.2007.10.043.

[55] Li X-y, Sun B-g, Zhang D-s, Wang X, et al. Experimental study on the cycle variation characteristics of direct injection hydrogen engine. Energy Convers Manag X 2022;15:100260. https://doi.org/10.1016/j.ecmx.2022.100260.

[56] Kosmadakis GM, Rakopoulos DC, Rakopoulos CD. Effect of two mechanisms contributing to the cyclic variability of a methane–hydrogen-fueled spark-ignition engine by using a fast CFD methodology. J Energy Eng 2023;149(1):04022058. https://doi.org/10.1061/JLEED9.EYENG-4620.

[57] Purayil STP, Al-Omari SAB, Elnajjar E. Effect of hydrogen blending on the combustion performance, emission, and cycle-to-cycle variation characteristics of a single-cylinder GDI spark ignition dual-fuel engine. Int J Thermofluids 2023;20:100403. https://doi.org/10.1016/j.ijft.2023.100403.

[58] Kosmadakis GM, Rakopoulos DC, Rakopoulos CD. Assessing the cyclic-variability of spark-ignition engine running on methane-hydrogen blends with high hydrogen contents of up to 50. Int J Hydrogen Energy 2021;46(34):17955–68. https://doi.org/10.1016/j.ijhydene.2021.02.158.

[59] Brunt MF, Emtage AL. Evaluation of Burn Rate Routines and Analysis Errors. SAE Technical Paper 970037. 1997. https://doi.org/10.4271/970037.

[60] Buzzi, L., Biasin, V., Galante, A., Gessaroli, D. et al., "Experimental investigation of hydrogen combustion in a single cylinder PFI engine," Presented at proceedings of 2022 thiesel congress, valencia..

[61] Bai-gang S, Hua-yu T, Fu-shui L. The distinctive characteristics of combustion duration in hydrogen internal combustion engine. Int J Hydrogen Energy 2014;39(26):14472–8. https://doi.org/10.1016/j.ijhydene.2014.04.013.